On Vanadium Substitution in Li_2MnSiO_4/C as Positive Electrode for Li-ion Batteries

Nils P. Wagner[1], Per Erik Vullum[2,3] Magnus Kristofer Nord[3,a], Ann Mari Svensson[1] and Fride Vullum-Bruer[1*]

[1]*Department of Materials Science and Engineering, NTNU, Norwegian University of Science and Technology,*

7491 Trondheim, Norway

[2]*SINTEF Materials and Chemistry, 7491 Trondheim, Norway*

[3]*Department of Physics, NTNU, Norwegian University of Science and Technology,*

7491 Trondheim, Norway

Abstract

Vanadium substitution is an interesting approach to manipulate the properties of the poor electronic and ionic conducting lithium transition metal orthosilicates. Especially, if incorporated on the Si-site it could alter the highly insulating character of the SiO_4 framework. This study addresses the feasibility and limitations of V substitution in Li_2MnSiO_4. Nominal compositions of $Li_2Mn_{1-x}V_xSiO_4$ ($0 \leq x \leq 0.2$) and $Li_2MnSi_{1-x}V_xO_4$ ($0 \leq x \leq 0.3$) were synthesized by a sol-gel method, and the structural evolution was analyzed by X-ray diffraction and transmission electron microscopy (TEM) coupled with electron energy loss spectroscopy (EELS). While the solid solubility of V on tetrahedral Mn-sites was shown to be limited, substantial amounts of V entered the structure when intended to substitute Si. Elemental mapping by TEM showed that V was highly inhomogeneously distributed and high energy resolution EELS demonstrated that the

majority of V was present in a tetravalent state. The nominal compositions $Li_2MnSi_{1-x}V_xO_4$ ($0 \leq x \leq 0.3$) showed superior electrochemical performance, with reduced charge transfer resistance and an increased Li-ion diffusion coefficient. Furthermore, cyclic voltammetry revealed increased redox activity which can be attributed to V within the concentration series. The best performance was achieved with 25 mol % V substitution. V substitution beyond 25 mol % caused deterioration of the properties.

[a] Present address: SUPA, School of Physics and Astronomy, University of Glasgow, Glasgow G12 8QQ, United Kingdom

[*] Corresponding author: +47 735 93976; fride.vullum-bruer@ntnu.no

Introduction

Environmentally benign lithium transition metal orthosilicates of the general formula Li_2MSiO_4 (M = Mn, Fe) have gained interest since Nytén *et al.* reported Li_2FeSiO_4 as cathode material for Li-ion batteries. [1] These polyanion compounds consist of abundant elements and allow in theory the reversible exchange of 2 Li ions per formula unit. [2–4] Li_2MnSiO_4 is an interesting candidate, since Mn can exist in different oxidation states (II, III, IV) within the potential window of a commercial Li-ion battery, thus gives rise to a high theoretical capacity of 333 $mAhg^{-1}$ for the exchange of 2 Li per formula unit. [5] Li_2MnSiO_4 adopts β and γ Li_3PO_4 structures where all cations are tetrahedrally coordinated. So far two orthorhombic (*Pmn2₁*, *Pmnb*) and two monoclinic (*P2₁/n*, *Pn*) polymorphs are known. Most syntheses include an annealing step at elevated temperatures between 600 and 800 °C and result in orthorhombic *Pmn2₁* or a mixture of *Pmn2₁* and *Pmnb*. [2,6–9] A major drawback of Li_2MnSiO_4 is the structural instability upon cycling

which is believed to be caused by cooperative Jahn-Teller distortions during oxidation. Both, tri- and tetravalent Mn are highly destabilized in a tetrahedral crystal field by the partial occupation of the energetically unfavorable t_2 orbitals. According to crystal field theory, trivalent and tetravalent would favor a square pyramidal or an octahedral environment, respectively. Recent computational studies by Saracibar *et al.* and Yi *et al.* revealed that the Mn coordination is likely to change upon oxidation. This results in a loss of the lithiation paths and of long-range order and hence causes severe capacity decay. [10,11] Furthermore, the rather insulating character and the low ionic conductivity of Li_2MnSiO_4 need to be addressed. Dominko *et al.* reported a low electronic conductivity of $3 \cdot 10^{-14}$ Scm^{-1} at 60 °C. [2] The reported Li ion diffusion coefficient ranges between 10^{-14} and 10^{-18} cm^2s^{-1}. [12,13] The reported values are some orders of magnitude lower than diffusion coefficients reported for Li_2FeSiO_4 and $LiFePO_4$. [14,15] DFT calculations by Kuganathan *et al*. further revealed a high activation energy barrier for Li ion migration of 0.95 eV in orthorhombic *Pmn2₁* Li_2MnSiO_4. [5] Means of remedying the conductivity issues have so far been to coat Li_2MnSiO_4 with a thin layer of conductive carbon. The aim of this coating is to enhance the electronic conductivity while keeping the particle size in the nanoregime in order to minimize the mean diffusion length of Li ions. [2,9,16,17] In addition, doping strategies on either the Mn-site or the Si-site are an interesting approach to manipulate the conductivity issues. It was pointed out that doping of trivalent Al on the Si-site is energetically favorable and would lead to charge compensation by interstitial Li ions. [5] Another approach is to synthesize lithium transition metal orthosilicates of the general formula $Li_2Mn_{1-x}Fe_xSiO_4$, with the aim to keep a high theoretical capacity by exploiting the 2 redox couples of Mn combined with the stability of Li_2FeSiO_4. [17–24] Li_2FeSiO_4 and Li_2MnSiO_4 crystallize both in β and γ Li_3PO_4 structures [4] and since Mn and Fe are direct neighbors in the periodic table, similarities can be expected. Another interesting candidate

for partial substitution of the transition metal or silicon in Li_2MSiO_4 compounds is vanadium. V is known as cathode material in the form of V_2O_5, [25–27] and according to resent DFT calculations up to 50 mol % V substitution on the Fe-site of Li_2FeSiO_4 is supposed to be stable and give rise to three additional redox couples. [28] Calculations by Liivat and Thomas suggest the possibility of a partial substitution of SiO_4^{4-} units by VO_4^{3-}, charge compensated by Li vacancies. [29] They also found the tetrahedral structure to stabilize VO_4^{4-}. Up to date, experimental studies of V doping in Li_2MSiO_4 compounds show inconsistencies and are not very thorough. A study by Yang *et al.* shows phase separation into V and Fe containing spinel phases at higher doping levels of V in Li_2FeSiO_4, and a general decay of the electrochemical properties. [30] Zhang *et al.* substituted up to 7 mol % V on the Fe-site of Li_2FeSiO_4 and found a strong increase of electrochemical properties for 5 mol % V substitution. [31] At the same time their XRD data shows that almost all major Li_2FeSiO_4 diffraction peaks diminish at increased V concentrations. The evolution of a spinel phase, with the main peak at about 35 ° 2Θ is ignored, and refinements based on the quality of their diffraction data are questionable. Hao *et al.* reported an increase in electrochemical performance when 10 mol % V are substituted on the Si-site of Li_2FeSiO_4, while substitution on the Fe site causes deterioration of the electrochemical properties. [14] This group also ignores the appearance of spinel peaks when part of the Fe is replaced by V. Both groups further confirmed trivalent V in their samples, when substitution was attempted on Fe-sites, by X-ray photoelectron spectroscopy (XPS). However, the measured signal could also be attributed to trivalent V from the ignored V containing spinel phases, since XPS does not allow for high spatial resolution. To the authors' knowledge there are so far no computational studies concerning V substitution in Li_2MnSiO_4. A broader doping study including up to 10 mol % V on either the Mn or the Si-site of Li_2MnSiO_4 by Deng *et al*. demonstrated an increased discharge capacity for 5 mol % V on

both sites, but deterioration for 10 mol % V. [32] We also previously reported improved electrochemical properties by the incorporation of 5 mol % V into the Mn or Si-site of Li_2MnSiO_4. [24] Another recent study by Hwang *et al.* reports up to 10 mol % V^{3+} substitution in Li_2MnSiO_4, and claims no redox contribution of V, but a positive effect on the Li diffusion coefficient. [13] Here, we report a more systematic study of the feasibility and limits of V substitution in Li_2MnSiO_4 and focus on whether it is possible to substitute Mn or Si by V. Samples with the nominal compositions $Li_2Mn_{1-x}V_xSiO_4$ ($0 \leq x \leq 0.2$) and $Li_2Mn_{1-y}Si_{1-x}V_xO_4$ ($0 < x \leq 0.3$) were prepared and characterized, with focus on the phase evolution as a function of V concentration. A combination of scanning TEM (STEM) and high energy resolution EELS was performed to determine the oxidation states and to map the distribution of V with high spatial resolution. Finally, the electrochemical properties as a function of the V content were examined.

Experimental:

Sample preparation

The Li_2MnSiO_4 reference sample was synthesized by an acidic PVA assisted sol-gel method using metal nitrates and TEOS as precursors. 0.03 mol $Mn(NO_3)_2$ * $4H_2O$ (Merck Ensure for analysis, > 98%) was dissolved in 25 mL deionized H_2O and 0.06 mol dried $LiNO_3$ (Alfa Aesar, 99 %) was added to the solution. The pH of the solution was set to ~1.5 by adding HNO_3 (Sigma Aldrich ≥ 65 % pro Analysi) in order to stabilize Mn^{2+} and control the gelation properties. A second solution consisting of 0.03 mol tetraethyl orthosilicate (TEOS) (VWR 99 %) and 20 mL EtOH was added drop wise to the metal cation solution under vigorous stirring. After 20 min

1.14 g PVA (Sigma Aldrich Mowiol 10–98, Mw =61,000) dissolved in 20 mL H_2O was added and the sol was left for gelation at 70 °C under slow stirring. The resulting gel was aged for 72 h at room temperature prior to drying at 120 °C in air and calcination at 450 °C for 1 h in flowing 5 % H_2 95 % Ar atmosphere. After calcination the precursor was wet mortared with 25 wt. % corn-starch as carbon source and EtOH as dispersant. The compound was finally heat treated for 10 h at 650 °C in flowing 5 % H_2 95 % Ar atmosphere to obtain the main phase and carbon coat the material in a single step. Further process details are published elsewhere. [33] Nominal compositions of $Li_2Mn_{1-x}V_xSiO_4$ ($0 \leq x \leq 0.2$) and $Li_2MnSi_{1-x}V_xO_4$ ($0 \leq x \leq 0.3$) were synthesized in the same manner, where either the Mn or Si precursor was partially substituted by equivalent molar concentration of V. The V precursor NH_4VO_3 (Sigma-Aldrich puriss p.a. > 99.5%) was dissolved under addition of 1.5 times the molar equivalent of oxalic acid (Sigma Aldrich puriss. p.a., anhydrous, ≥ 99.0 %) in 15 mL deionized H_2O. The solution was left to react for 1 h before it was mixed with a 15 mL H_2O solution containing $LiNO_3$ and $Mn(NO_3)_2 * 4H_2O$. TEOS and PVA solutions were added in the same manner as for the reference sample, and the sol was left to gel as described above. Gel ageing, drying, calcination and reduction parameters were the same as for the reference.

Characterization

Structural analysis was performed by powder X-ray diffraction using a Bruker D 8 Advance Da-Vinci working in Bragg–Brentano (Θ/2Θ) geometry. Powder XRD patterns were recorded from 2Θ = 15–75° under CuK_α radiation, with a step-size of 0.013 ° and an integration time of 0.75 s, using a variable slit setup. The structure of Li_2MnSiO_4 was fitted to the space group *Pmn2₁* using

Topas (Bruker AXS Version 4.2). The starting model was proposed by Li *et al*. [34]. The nominal compositions $Li_2MnSi_{1-x}V_xO_4$ ($0 \leq x \leq 0.3$) were fitted to this model, disregarding the substituted V in the model. Surface area and porosity data were acquired, by nitrogen adsorption according to BET, T-plot and BJH theory, on a Micrometrics Tristar 3000. The powder was vacuum dried for 24 h at 250 °C prior to analysis. Further morphological and structural analysis was carried out by (scanning) transmission electron microscopy ((S)TEM). The powder samples were dispersed in ethanol, and a droplet was transferred to a holey carbon coated Cu TEM grid. Prior to TEM characterizations, the samples were gently plasma cleaned 2·10 s inside a shielding port by a Fischione plasma cleaner to remove possible contaminations. TEM was performed with a double Cs corrected, coldFEG JEOL ARM200CF, operated at 200 kV and equipped with a Gatan Quantum ER for electron energy loss spectroscopy (EELS) and a large solid angle (98 srad) Centurio detector for X-ray energy dispersive spectroscopy (EDS). Spectroscopy (both EDS and EELS) was performed with a 27 mrad convergence semi-angle and a 384 pA probe current. Sub-pixel scanning was always applied to have an effective exposure time of less than 200 µs in every location of the map to avoid possible beam damage. Elemental mapping by EELS was performed with an energy dispersion of 1 eV/channel and a collection semi-angle of 66 mrad. High energy resolution EELS was performed with an energy dispersion of 0.1 eV/channel, a collection semi-angle of 33 mrad, and an energy resolution of 0.6 eV. Dual EELS (two EEL spectra were acquired in every pixel of the maps) was used for the fine structure analysis of the V and Mn $L_{2,3}$ EEL white lines. The low loss spectrum, including the zero loss peak, was used to calibrate the energy scale and to allow for the low loss plasmon signal to be convolved with the core loss Mn and V $L_{2,3}$ peaks to account for multiple scattering. The EELS maps were in general

processed with a model based approach [35] using the open source software HyperSpy. [36] Two Hartree-Slater edges were used to model the L_2 and L_3 ionization edges for both V and Mn. [37]

Electrochemical characterization

For electrochemical characterizations cathodes were produced by tape casting an N-Methyl-2-pyrrolidone (NMP Sigma Aldrich > 99 %) based slurry on Al foil as current collector. The slurry contained 85 wt. % active material, 10 wt. % conductive carbon (Super P Li, Timcal) and 5 wt. % Polyvinylidene fluoride (PVDF) (Kynar, reagent grade) as binder. Cast thicknesses were 15-20 μm and the solid load was about 2 mg cm^{-2}. CR2016 coin cells were assembled in a glove box (dry Ar atmosphere) using a 16 mm circular cathode, a Celgard 2400 separator and a circular Li metal disc as anode. The electrolyte consisted of 1 M $LiPF_6$ dissolved in a 1:1 volume ratio of Ethylene carbonate / Diethyl carbonate solution (Aldrich Battery grade). Furthermore, three electrode set-ups were assembled using ECC-Ref 3 electrode test cells from EL-cell. For the three electrode set-up Li was used as counter and reference electrode. The separator was a 1.55 mm thick glass fiber disc. To protect the cathode from the sharp fibers a Celgard separator was placed between the cathode and the glass fiber.

Galvanostatic cycling was performed on a LANHE CT 2001A in the potential window of 1.5 – 4.7 vs. Li/Li^+ at room temperature. Specific capacities are reported with respect to the mass of the corresponding carbon coated composites. To have a more comparable charge rate, only the one electron reaction of Mn^{2+}/Mn^{3+} was taken into account, and for mathematical simplicity the charge rate was defined as a current density of 160 mAg^{-1} = 1C.

Cyclic voltammograms (CV) and AC impedance spectroscopy data were measured on a Princeton Applied Research Parstat 4000 potentiostat at room temperature. CV sweep rate was 0.1 mVs^{-1} in a potential window of 1.5 – 4.7 vs. Li/Li^+. Impedance data were collected at open circuit potential (OCP). The amplitude of the alternating current (AC) signal was set to 10 mV in an AC frequency range of 10 KHz to 10 mHz.

Furthermore, *in situ* XRD experiments to examine the structural changes upon cycling were conducted during the first two galvanostatic cycles of Li_2MnSiO_4 and $Li_2MnSi_{0.75}V_{0.25}O_4$. Pouch cells were assembled using the same electrodes, separator and electrolyte as previously described. Cycling was performed on a Princeton Applied Research Parstat 4000 at C/16 in a potential window of 1.5 – 4.7 vs. Li/Li^+. The XRD patterns were recorded continuously on a Bruker D 8 Advance Da-Vinci with a LynxEye Xe detector working in Bragg–Brentano (Θ/ 2Θ) geometry using Mo K_α radiation in transmission mode. The additional layers of Al, PE, PP and Li that the beam had to penetrate in transition mode, limited the observable 2Θ region without interference from the cell components. Scans were recorded from 11.7 to 15.8 ° 2Θ (step-size of 0.015 °, integration time 3 s).

Results and discussion

Phase evolution and powder morphology dependency on the V concentration

The applied V precursor initially contains pentavalent V. Oxalic acid was added to ensure an acidic media in order to suppress the formation of V polyions and the oxidation of divalent Mn.

The reducing character of oxalic acid further caused a partial reduction of V to a tetravalent oxyion, visible through a color change from yellow to a deep bluish green solution. Upon gelation under atmospheric conditions V is reoxidized, visible by another color change back to yellow. All dried gels were mainly amorphous. However, some gels showed minor $LiNO_3$ precipitations. Figure 1 shows XRD patterns of the thermal history of the carbon coated Li_2MnSiO_4 sample, which was used as reference. During calcination the crystallization of Li_2SiO_3 and spinel phases occurs. After the calcined sample is mixed with corn-starch as carbon former and heat treated at 650 °C, mainly Li_2MnSiO_4 in the space-group *Pmn2₁* is present. Additionally, minor traces of MnO and Li_2SiO_3 were detected. The appearance of minor secondary phases is often reported for Li_2MnSiO_4. [9] It is most probably due to an uncompleted phase formation, which can be explained by sluggish kinetics in this complicated quaternary oxide.

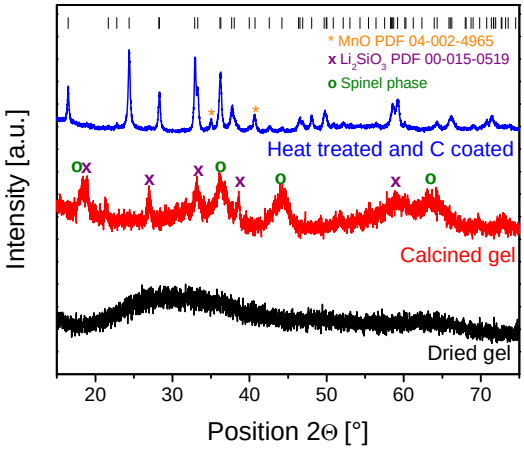

Figure 1: Powder XRD patterns of the Li_2MnSiO_4 reference sample after gel drying, after calcination, and after final heat treatment and C coating. Phases are denoted and Li_2MnSiO_4 $Pmn2_1$ bragg reflections are included.

The powder XRD patterns of the nominal compositions $Li_2Mn_{1-x}V_xSiO_4$ ($0 \leq x \leq 0.2$), magnified areas 26 to 30.5 and 54 to 65 ° 2Θ and the crystal structure including the *010*, *011* and *002* lattice planes are given in Figure 2 a), Figure 2 b) and Figure 2 c). The V concentration was progressively increased in 5 mol % steps until 20 mol %. A clear increasing trend in secondary phases is visible. Next to the previously mentioned Li_2SiO_3 and MnO, an increasing amount of a V rich spinel phase was detected, indicating the limited solubility of V on the Mn-site of Li_2MnSiO_4. The magnified areas 26 to 30.5 and 54 to 65 ° 2Θ show an increase in the intensity of the spinel and Li_2SiO_3 peaks, while the *200* diffraction line of Li_2MnSiO_4, although steady in position, is strongly decreasing in intensity and at the same time broadening. Reduced intensities were also detected for the *010, 011* and *002* reflections at 16.4, 24.4 and 36.2 ° 2Θ, respectively. Both the *010* and *011* lattice planes offer a high electron density mainly due to Mn, which is the heaviest atom of the structure and hence exhibits the highest electron density. The same is valid for the *200* plane, but for clarity of the figure, the illustration of the *200* plane was ignored. The observations of decreasing peak intensities from Bragg scattering by planes with a high electron density governed by Mn, while the amount of a V and Mn containing spinel phase is increasing, leads to the conclusion that the V solid solubility on the Mn-site is very limited. Elevated concentrations of V, which is octahedrally coordinated and trivalent in the spinel phase, [38] do not populate the tetrahedral Mn-sites but rather cause phase separation. In fact, the apparent decrease of the *002* intensity at higher V concentrations, suggests a highly defective $Li_2Mn_{1-x}SiO_4$ structure. Similar observations were made by Yang *et al.* for V substitution on the Fe-site of Li_2FeSiO_4. [30] As previously mentioned, other authors ignored the presence of spinel diffraction lines in their diffractograms when they claimed V substitution on the transition metal-site of both Li_2FeSiO_4 and Li_2MnSiO_4. [14,31,32] The increased amount of Li_2SiO_3 is correspondingly

inevitable, since the transition metal concentration necessary to form the main phase is decreased.

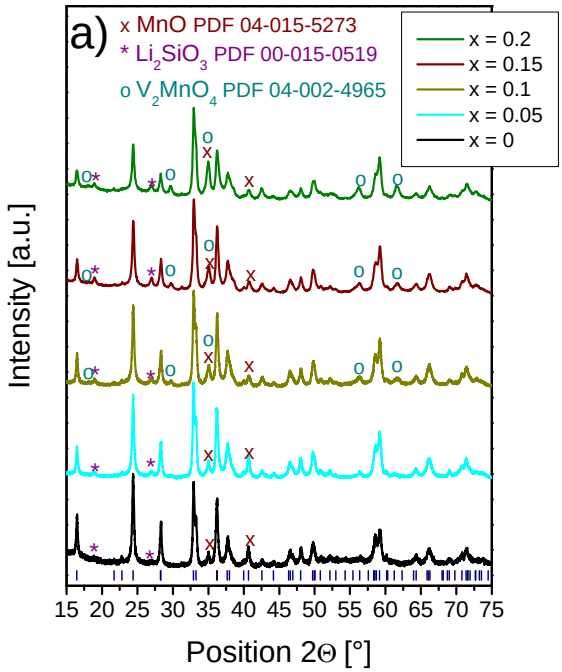

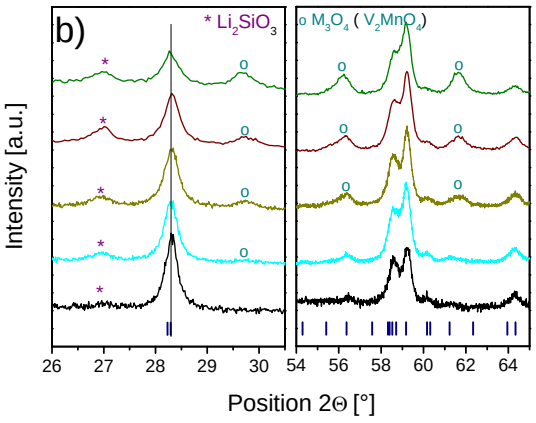

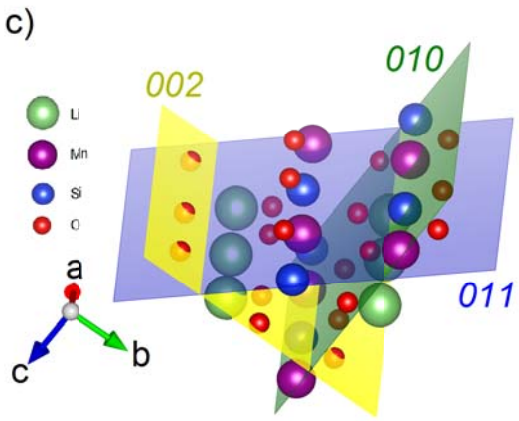

Figure 2: a) Powder XRD patterns of the nominal compositions $Li_2Mn_{1-x}V_xSiO_4$ ($0 \leq x \leq 0.2$) including denotation of secondary phases and Li_2MnSiO_4 *Pmn2₁* bragg reflections. b) Magnification of the corresponding powder XRD patterns in the range of 16-30.5 and 54-65 2Θ with a clear increase in a V and Mn containing spinel phase and Li_2SiO_3.c) Lattice planes of the Li_2MnSiO_4 *Pmn2₁* structure corresponding to the peaks that show a reduced intensity with increasing V concentration.

Contrary to the observations made for $Li_2Mn_{1-x}V_xSiO_4$, the nominal compositions $Li_2MnSi_{1-x}V_xO_4$ ($0 \leq x \leq 0.3$) show no evidence of V rich spinel phases. The patterns were fitted to a Li_2MnSiO_4 model. The nanocrystalline character in combination with a substantial amount of carbon cause broad peaks and a low signal to noise ratio, which make a reasonable fit challenging. The incorporation of V into the elaborated model, in order to find the site occupancy, did not deliver meaningful insights and hence is omitted. Figure 3 a) shows the corresponding fitted powder XRD patterns. A magnified region from 16 to 23.4 ° 2Θ is shown in Figure 3 b).

The intensities of the diffraction lines corresponding to a cubic, rock-salt structured MnO related phase are increasing, and the peak shapes are broadening at higher V concentrations. Further

observations were irregular changes in peak intensities and substantial increased intensities of the *Pmn2*$_1$ *110* and *101* diffraction lines. Moreover, the position of the former changed within the concentration series. If it is assumed that V occupies Si-sites, Bragg scattering from Si-rich planes should increase in intensity, since V has a higher scattering power than Si due to the higher atomic number. Significant changes in the *110* and *101* diffraction lines which correspond mainly to Li, hence indicate increasing disorder in the crystal structure, as well as local deviations and distortion of the unit cell which could lead to a lowered symmetry. The increased intensity of the two diffraction lines could indicate a partial Li-V or Li-Mn site reversal with increasing V concentration. Cation site-reversal is observed in Li_2FeSiO_4. The material undergoes a transition to an inversed β_{II} structure, which is similar to the structure of Li_2MnSiO_4, but Fe occupies half the Li-sites. The reversal causes increased intensities of the *110* and *101* diffraction lines. [39] *Pmn2*$_1$ lattice parameters, the calculated crystallite size, and the carbon content from TGA analysis are given in Table 1. The lattice parameters of the concentration series show a minor inconsistent trend to an increased cell volume. This observation was unexpected, since even pentavalent V has a bigger ionic radius than Si, and should influence the lattice parameters more pronounced if V solely occupies one crystallographic site. Crystallite sizes were calculated to range between 36-56 nm from the full width at half maximum of the *011* peak. The calculations accounted for peak shape broadening due to strain. The calculated crystallite sizes are comparable. One exception is the 15% sample, which shows the biggest crystallites with 56 nm. The carbon contents are comparable The same was valid for the nominal compositions $Li_2Mn_{1-x}V_xSiO_4$ ($0 \leq x \leq 0.2$) where the estimated carbon contents from TGA data also ranged between 4 and 5 wt. %.

Table 1: Lattice constants and XRD crystallite sizes of the nominal compositions $Li_2MnSi_{1-x}V_xO_4$ ($0 \leq x \leq 0.3$)

x in $Li_2MnSi_{1-x}V_xO_4$	A[Å]	B[Å]	C[Å]	Cell volume [$Å^3$]	Crystallite size [nm]	Carbon content [wt. %]
0	6.30499(85)	5.38475(78)	4.96513(66)	168.570(40)	41.1	6
0.05	6.3041(12)	5.38533(91)	4.96266(88)	168.481(52)	37.9	5
0.1	6.30693(95)	5.38441(82)	4.96386(73)	168.568(44)	38.5	5
0.15	6.3038(12)	5.3859(11)	4.9640(11)	168.538(61)	55.8	4
0.2	6.3043(14)	5.3844(14)	4.9622(13)	168.442(73)	42.5	4
0.25	6.30972(96)	5.38682(84)	4.96421(75)	168.730(45)	36.2	5
0.3	6.3094(12)	5.3889(10)	4.96461(93)	168.801(55)	36.6	5

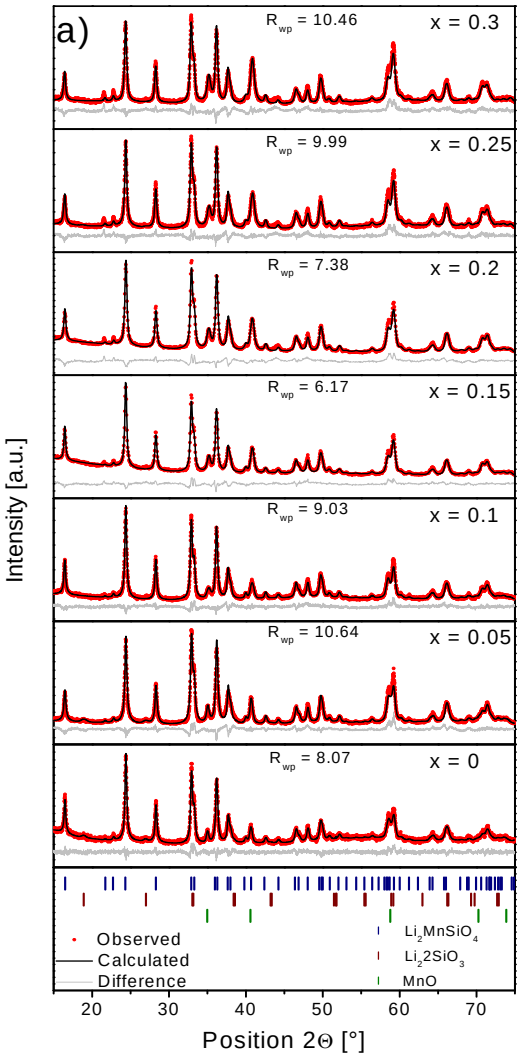

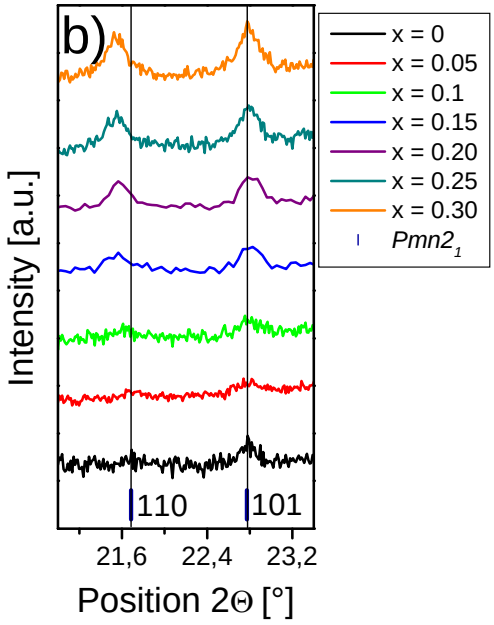

Figure 3: a) Fitted powder XRD patterns of the nominal compositions $Li_2MnSi_{1-x}V_xO_4$ ($0 \leq x \leq 0.3$) including Li_2MnSiO_4 *Pmn2₁*, Li_2SiO_3 and MnO Bragg reflections. b) Highlighted area from 21 to 23.4 ° 2Θ including the *110 101 Pmn2₁ hkl* positions and a vertical line as a guide for the eye.

Since the XRD patterns of the nominal compositions $Li_2MnSi_{1-x}V_xO_4$ ($0 \leq x \leq 0.3$) suggest incorporation of V into the structure, further physio-chemical characterization was focused on these samples. To gain a deeper understanding of how V is incorporated into the structure STEM EELS spectral maps of the nominal compositions Li_2MnSiO_4, $Li_2MnSi_{0.9}V_{0.1}O_4$ and $Li_2MnSi_{0.75}V_{0.25}O_4$ were acquired. The set-up described in the experimental section was carefully chosen to hinder beam damage during acquisition, since V is prone to reduction if exposed to the high energy electron beam for prolonged times. [40,41] The elemental distribution of Li, Mn, Si and O was homogenous in all cases, and except for the carbon coating no amorphous areas were

detected. Figure 4 a) and Figure 4 b) show high angle annular dark field (HAADF) STEM images of agglomerates with the nominal compositions $Li_2MnSi_{0.9}V_{0.1}O_4$ and $Li_2MnSi_{0.75}V_{0.25}O_4$, respectively. Red dotted lines indicate the areas where EELS maps were acquired. The corresponding V maps, made from the V $L_{2,3}$ peaks, are shown in Figure 4 c) and Figure 4d).

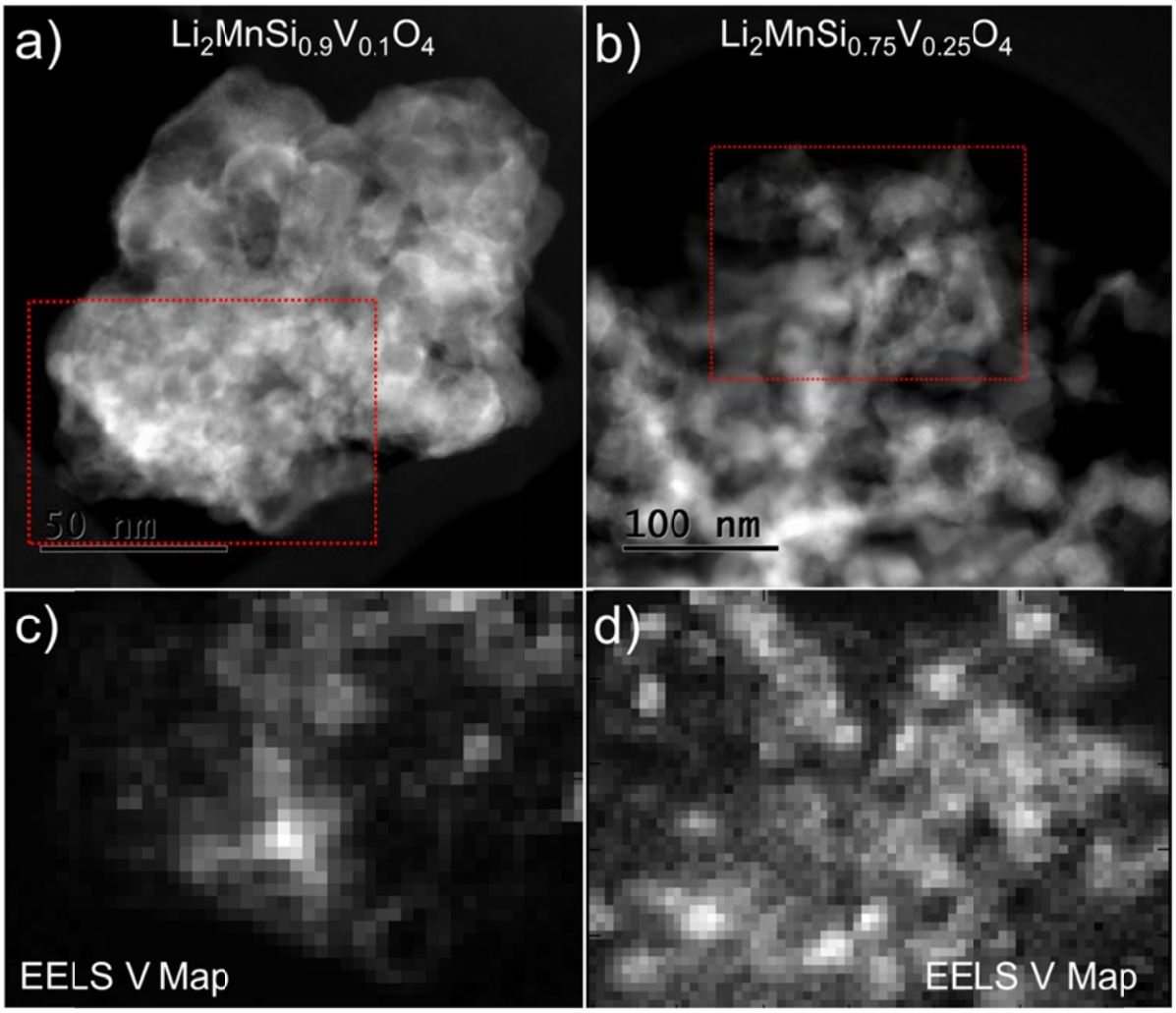

Figure 4: HAADF STEM micrographs of the nominal compositions a) $Li_2MnSi_{0.9}V_{0.1}O_4$ and b) $Li_2MnSi_{0.75}V_{0.25}O_4$. The regions for EELS spectrum imaging are highlighted. V maps of c) $Li_2MnSi_{0.9}V_{0.1}O_4$ and d) $Li_2MnSi_{0.75}V_{0.25}O_4$.

The results indicate that V is incorporated into the structure, but in both cases the distribution of V in the samples is highly inhomogeneous, where distinct areas show much higher V concentrations. These V inhomogeneities will have a major influence on the local compositions of the materials and probably cause numerous defects like stacking faults and local breaches of symmetry, which could explain the increase in misfit of the XRD pattern with increasing V concentration. In fact, if strain effects were disregarded during crystallite size calculations, the calculated values of V substituted samples ranged from 27 to 25 nm. The primary oxidation state of V was in both samples the same, but the 10 mol % and the 25 mol % samples showed some differences with respect to the second oxidation state that was observed. Figure 5 a) and Figure 5 b) show the V $L_{2,3}$ edges from the 10 mol % and the 25 mol % samples with corresponding Mn $L_{2,3}$ edges from the same pixels in the spectrum images as the main V signal. The most representative V spectrum, i.e. the most commonly observed oxidation state in the acquired spectrum images, is shown as a solid black line. The second, but less common V oxidation state, present in each of the samples, is shown by dashed blue lines.

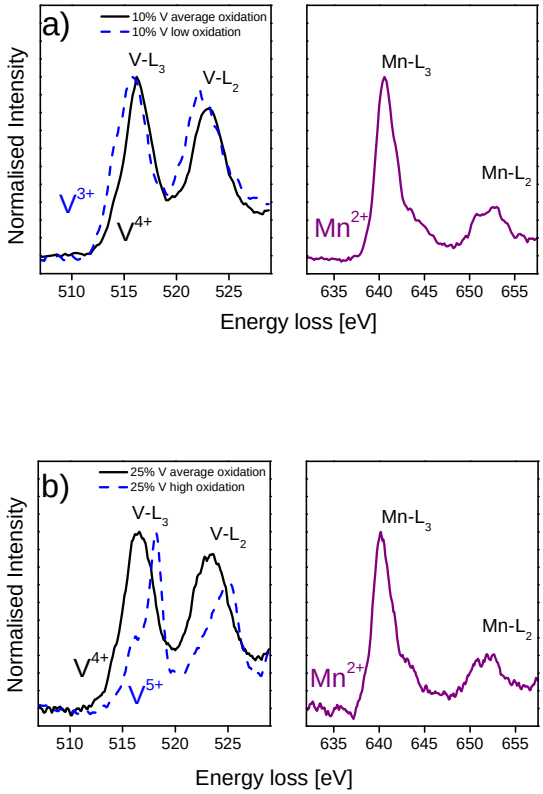

Figure 5: Most representative V $L_{2,3}$ (solid black line)and the corresponding Mn $L_{2,3}$ peaks acquired from the same pixel of the spectrum images of the nominal compositions a) $Li_2MnSi_{0.9}V_{0.1}O_4$ and b) $Li_2MnSi_{0.75}V_{0.25}O_4$. The minor V $L_{2,3}$ peaks(dashed blue line) are recorded from different pixels.

Careful analysis of the energy loss at the peak onset, the shape of the fine structure, and comparison to data from other well established microscopy research groups [42,43] strongly suggest the majority of V to be present in a tetravalent state. In fact, Liivat and Thomas suggested the tetrahedral structure offering a stabilizing effect on VO_4^{4-} units. [29] Differences were detected in the second, but less common V oxidation states that were seen in each of the samples. In the case of $Li_2MnSi_{0.9}V_{0.1}O_4$ the minority oxidation state was characterized by a $L_{2,3}$ peak that was shifted

towards a lower energy loss, and the difference in onset was ~0.8 eV. In $Li_2MnSi_{0.75}V_{0.25}O_4$ the opposite trend was observed. A second oxidation state characterized by a $L_{2,3}$ peak that was shifted about 1.2 eV in onset towards higher energy, was present. These chemical shifts correlate excellently with reported values, [42] and can be attributed to small amounts of trivalent V present in $Li_2MnSi_{0.9}V_{0.1}O_4$ and pentavalent V in $Li_2MnSi_{0.75}V_{0.25}O_4$. The fine structure of Mn in close neighborhood to the measured V signal, can be clearly attributed to divalent Mn. [42] However, also minor fractions of trivalent Mn were detected in all the samples. Tetravalent V would not require any charge compensation if located on vacant Si-sites. However, the inhomogeneous distribution and the changes in the XRD patterns indicate considerable disorder. The V signals corresponding to a different valence require charge compensation. A lower valence could be compensated by partly oxidation of Mn to a trivalent state. Pentavalent V on the other hand would require the formation of vacancies in the Li or Mn sub-lattice. We recently reported the possibility of Li_2MnSiO_4 being stable in a slightly Mn deficient state. [44] Furthermore, EDS mapping of Mn and O rich particles, which can be attributed to the MnO related phase, also showed considerable amounts of V. This suggests that the secondary phase detected by XRD should be more correctly addressed as rock-salt structured $Mn_{1-x}V_yO$ ($1-x+y < 1$). MnO phases are well known to exist as cation sub-stoichiometric oxides, and could very possibly accommodate limited V amounts. If the increase in the secondary phase is due to a thermodynamic limit of V substitution or the thermal and atmospheric history of the samples cannot be concluded. The highly reducing atmosphere during heat treatment could cause partial reduction of the initially pentavalent V to a trivalent state, and our findings suggest only limited solubility for the trivalent ion. A non-stoichiometric situation may occur if parts of the reduced V cannot be incorporated into the structure. This resulting non-stoichiometry would then cause

segregation of the excess Mn and Li. Combining the findings of a non-homogeneous V distribution as well as minor amounts of V in a different valence state leads to the conclusion of varying local compositions which could explain the fact that it was not possible to elaborate a meaningful Rietveld model with increasing V concentration. It could also explain why no substantial increase in cell volume was detected. The X-ray diffractograms give most probably a highly strained average of locally very different compositions, which can still fairly well be described by the *Pmn2$_1$* space group. The inhomogeneous character, the different oxidation states of V, and the increasing amount of the $Mn_{1-x}V_yO$ (1-x+y < 1) will cause significant amounts of point defects and defects of a higher order in the structure. Hence it might alter the electronic structure of the material and possibly also affect the Li diffusion.

TEM bright field micrographs of the nominal compositions Li_2MnSiO_4 and $Li_2MnSi_{0.75}V_{0.25}O_4$, and vertically aligned electron diffraction patterns of the samples are shown in Figure 6 a) Figure 6 b) and Figure 6 c). Electron diffraction patterns were taken from large agglomerates (regions 1.5 µm in diameter containing several hundred single crystals) to visualize an average which allows for comparison. The powders consist of loosely agglomerated nanoparticles with an overall similar morphology. Primary particles range in both cases from 25 to 40 nm validating the crystallite sizes calculated from XRD data. The particles are surrounded by a thin layer of amorphous carbon, which was intended in order to increase the electronic conductivity of the materials. More detailed TEM images, which clearly show the amorphous carbon coating, can be found in an earlier work on the synthesis and characterization of the LMS reference sample. [33] The electron diffraction pattern of the reference and the 25 mol % V sample are comparable and no extra diffraction rings could be detected. They hence strengthen the assumption of a system that can be overall still described by the orthorhombic *Pmn2$_1$* structure.

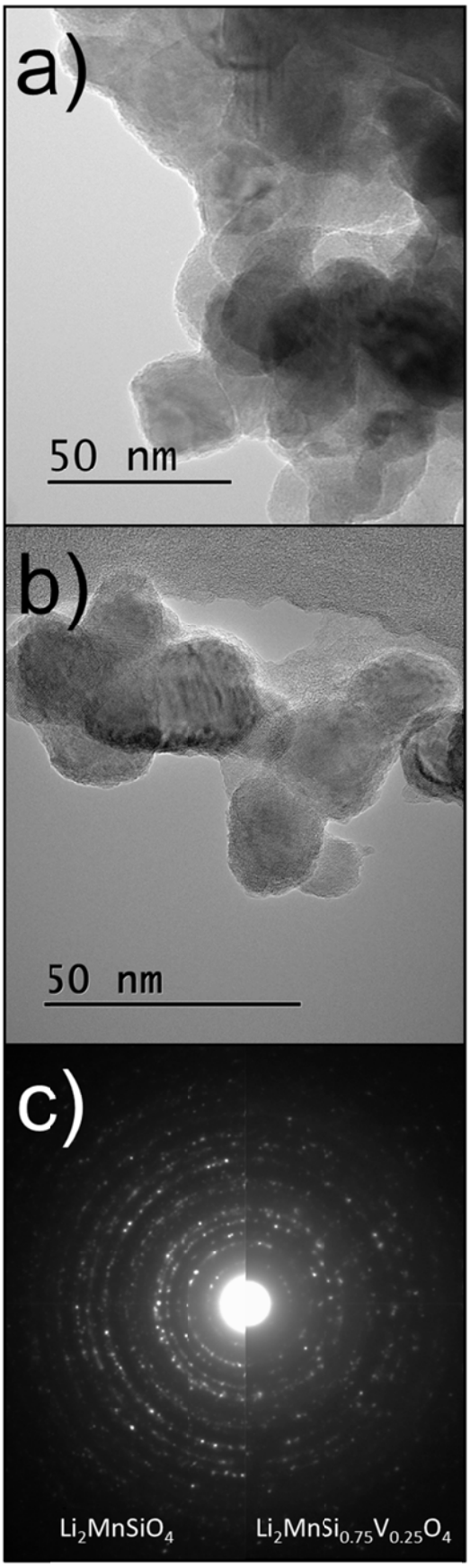
a)
50 nm
b)
50 nm
c)
Li_2MnSiO_4
$Li_2MnSi_{0.75}V_{0.25}O_4$

Figure 6: TEM bright field micrographs of the nominal compositions a) Li_2MnSiO_4 and b) $Li_2MnSi_{0.75}V_{0.25}O_4$. c) show a vertically aligned electron diffraction pattern taken from bigger agglomerates of Li_2MnSiO_4 and $Li_2MnSi_{0.75}V_{0.25}O_4$.

The surface area was measured according to T-plot theory which allows to divide the data into micropore area (pores < 2nm) and external surface area. Furthermore, the pore-size distribution was calculated from the BJH desorption data of the $Li_2Mn_{1-x}V_xSiO_4$ concentration series. The results are summarized in Figure 7 a) and Figure 7 b).

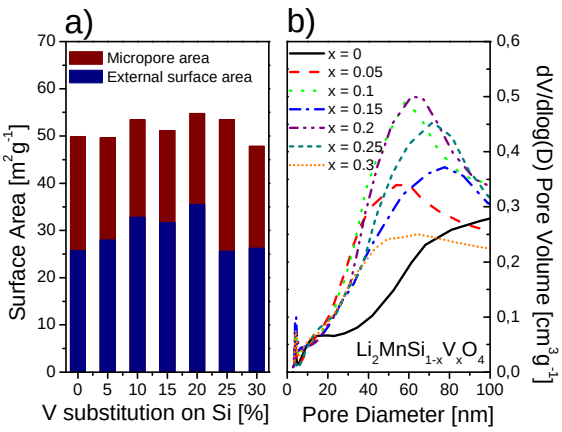

Figure 7: a) BET surface area divided into micropore area and external surface area of the $Li_2Mn_{1-x}V_xSiO_4$ samples. b) Pore-size distribution of the $Li_2Mn_{1-x}V_xSiO_4$ samples.

The external surface area shows an increase up to 20% V substitution, for higher substitution levels it decreases again to the value of the reference sample. The micropore area shows an opposing trend so that the overall surface area of the samples stays similar with values around 50 m^2g^{-1}. The inaccuracy of the method has a proportional trend with the surface area values, and

TEM suggested rather comparable morphologies. The pore size distribution data shows slight changes towards a smaller mean pore diameter. The morphology of V substituted samples appears to be rather similar and hence cannot be used to explain any major differences in the electrochemical properties.

Electrochemical analysis

The performance of $Li_2Mn_{1-x}V_xSiO_4$ ($0 \leq x \leq 0.15$) and $Li_2MnSi_{1-x}V_xO_4$ ($0 \leq x \leq 0.3$) were assessed by galvanostatic cycling. Analysis of the nominal composition $Li_2Mn_{0.8}V_{0.2}SiO_4$ was omitted since phase separation was already predominant. The first charge and discharge curves of the samples are shown in Figure 8 a) and Figure 8 b). While Figure 8 c) shows the rate performance of $Li_2MnSi_{0.75}V_{0.25}O_4$. All experiments were carried out at room temperature.

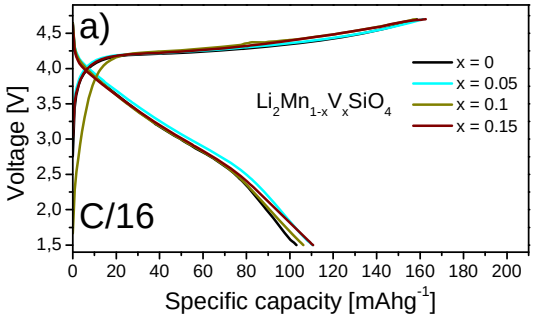

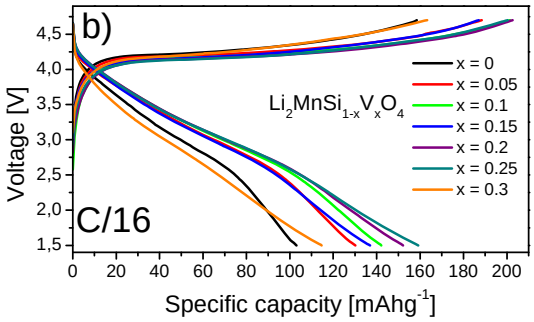

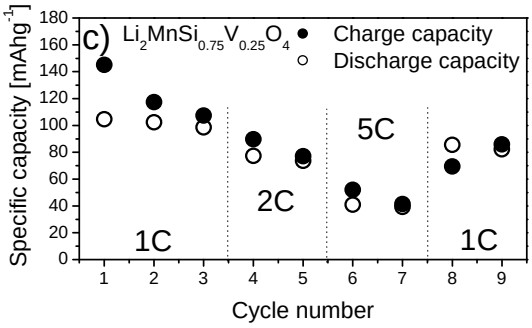

Figure 8: First galvanostatic cycle at C/16 and room temperature of a) $Li_2Mn_{1-x}V_xSiO_4$ ($0 \leq x \leq 0.15$) and b) $Li_2MnSi_{1-x}V_xO_4$ ($0 \leq x \leq 0.3$). c) $Li_2MnSi_{0.75}V_{0.25}O_4$ cycled at different rates.

Substitution of V on the Mn-site did not show significant changes in the charge/discharge behavior. The charge capacity was in all cases about 160 $mAhg^{-1}$, and the corresponding discharge showed capacities ranging between 100 and 110 $mAhg^{-1}$. This corresponds to an irreversible loss of about 35%. Interestingly, the capacity is not decreasing with increasing phase separation. This could be caused by the highly defective structure showing higher Li diffusion. Also, it is not excluded that small amounts of V could be offering additional redox activity in the structure. However, V substitution on the Si-site showed a major impact on the electrochemical response of the system. The first charge and discharge capacity increased within the

concentration series and peaked at 25 mol % V. Only the 15 mol % sample was an exception and showed a slightly decreased capacity compared to the 10 mol % sample. XRD data suggested the crystallite size of this sample to be significantly larger, which could have a negative influence on the charge discharge characteristics of this sample. Furthermore, the measured carbon content with only 4 wt. % was one of the lowest in the series and could influence the electronic conductivity, hence it cannot be excluded that the decreased capacity at the given C rate is due to irregularities in the thermal history of the sample. The charge capacity of the 25 mol % sample was 25% higher, and the discharge capacity about 60% higher compared to the values of the reference sample. The irreversible capacity loss hence is decreased to a value of 20%. However, the sloping discharge profile suggests the known structural collapse of Li_2MnSiO_4 to occur also in V substituted samples. The lowered irreversible loss could be caused by larger VO_4 units keeping the structure more open and hence allow more relithiation. 30 mol % V substitution caused the discharge capacity to decrease again to about 115 $mAhg^{-1}$. It should be kept in mind that the amount of the dense rock-salt structured $Mn_{1-x}V_yO$ phase is increasing within the series, and will at some point influence the amount of electrochemically active material available. An interesting feature of the discharge curve of the V substituted samples is the less pronounced kink occurring at about 2.5 V. Figure 8 c) shows the rate capability of $Li_2MnSi_{0.75}V_{0.25}O_4$ at 1C, 2C and 5C. The sample delivers a comparable capacity at 1C as the reference sample at C16. The rate performance of Li_2MnSiO_4 is rather poor, as previously reported. [33] To understand the structural changes upon charging, *in situ* XRD patterns were recorded of Li_2MnSiO_4 and $Li_2MnSi_{0.75}V_{0.25}O_4$ upon galvanostatic cycling. *In situ* cycling was carried out in pouch cells consisting of polyethylene coated aluminum. The observed capacities in this set-up were slightly lower than the capacities measured in CR 2016 coin cells. The difference is most probably due to

an inhomogeneous pressure distribution and contacting in the in house made pouch cells. The limited interference free 2Θ region allowed the observation of the *Pmn2$_1$ 111/200* and *210/020* double peaks. To keep an adequate time resolution, the scan time was limited to about 22 min per scan, while the cells were cycled at a slow rate of C/16. To increase the readability, the results are presented as level plots in Figure 9 a) and Figure 9 b).

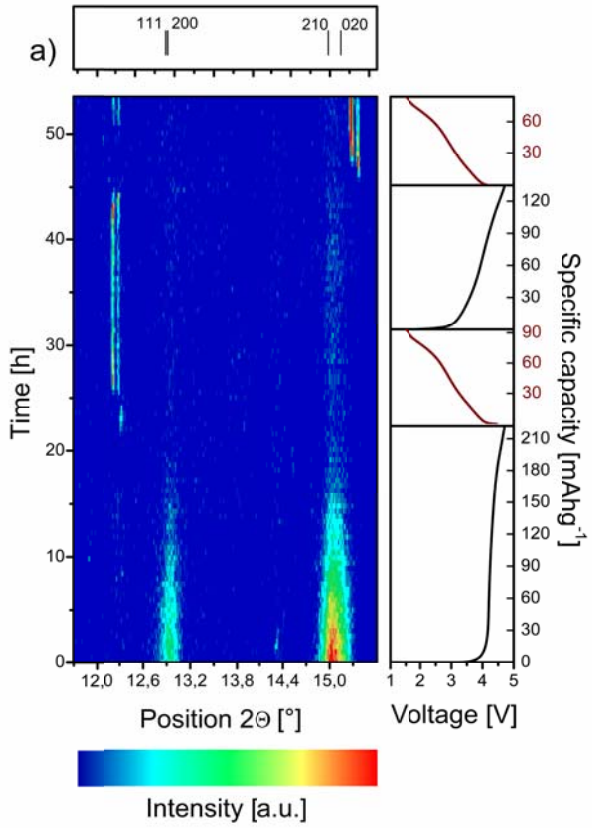

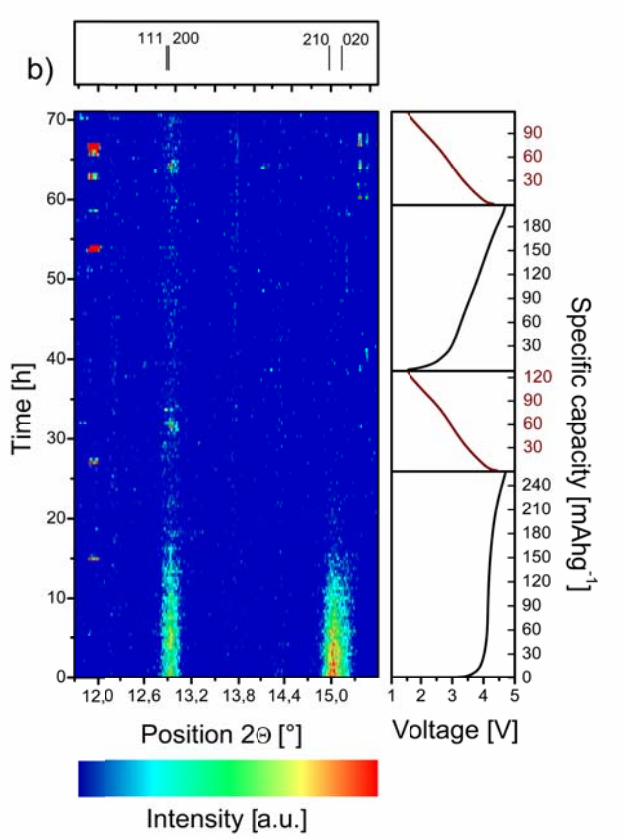

Figure 9: *In situ* XRD upon the first two galvanostatic cycles at C/16 for a) Li_2MnSiO_4 and b) $Li_2MnSi_{0.75}V_{0.25}O_4$.

The *in situ* analysis revealed that the peak intensity of both the reference sample and the 25 mol % V substituted sample is decreasing upon the first oxidation. In both cases the diffraction lines corresponding to the *Pmn2₁* structure diminish into the background noise at capacities close to the value of the one electron reaction. According to crystal field theory, trivalent Mn is highly destabilized in a tetrahedral field. Distortions or changes in coordination would stabilize the Mn center but could lead to a loss of long range order. The amorphization was shown to be irreversible since none of the corresponding peaks reappears upon reduction or the subsequent

cycle. In both cases some other peaks appear and disappear. The limited measurement window did not allow indexing of these diffraction lines. Furthermore, it cannot be concluded that these peaks appear on the cathode side since the scan was performed in transition mode. The multiple layers that had to be penetrated also limit the resolution of the *in situ* measurement. To confirm that the observed disappearance of the two double peaks is representative, the cells were disassembled and Cu K_α XRD scans were recorded of the cathodes. In both cases only very minor peaks corresponding to the *Pmn2₁* structure could still be detected in a highly amorphous matrix, confirming the nearly complete loss of long-range order after the initial charge. This confirms that V does not contribute to any stabilization of the structure upon cycling. To address the question if V shows electrochemical activity in $Li_2MnSi_{1-x}V_xO_4$, or if the increased activity is caused by increased conductivity of the materials, cyclic voltammograms were recorded. Figure 10 a) and Figure 10 b) show the voltammograms of the first and second cycle of $Li_2MnSi_{1-x}V_xO_4$ ($0 \leq x \leq 0.3$). Further shown are galvanostatic long-term cycling data of Li_2MnSiO_4 and $Li_2MnSi_{0.75}V_{0.25}O_4$ and differential capacity plots of various cycles in Figure 10 c) and Figure 10 d).

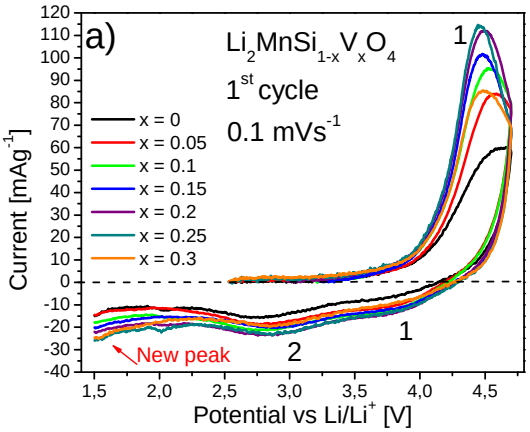

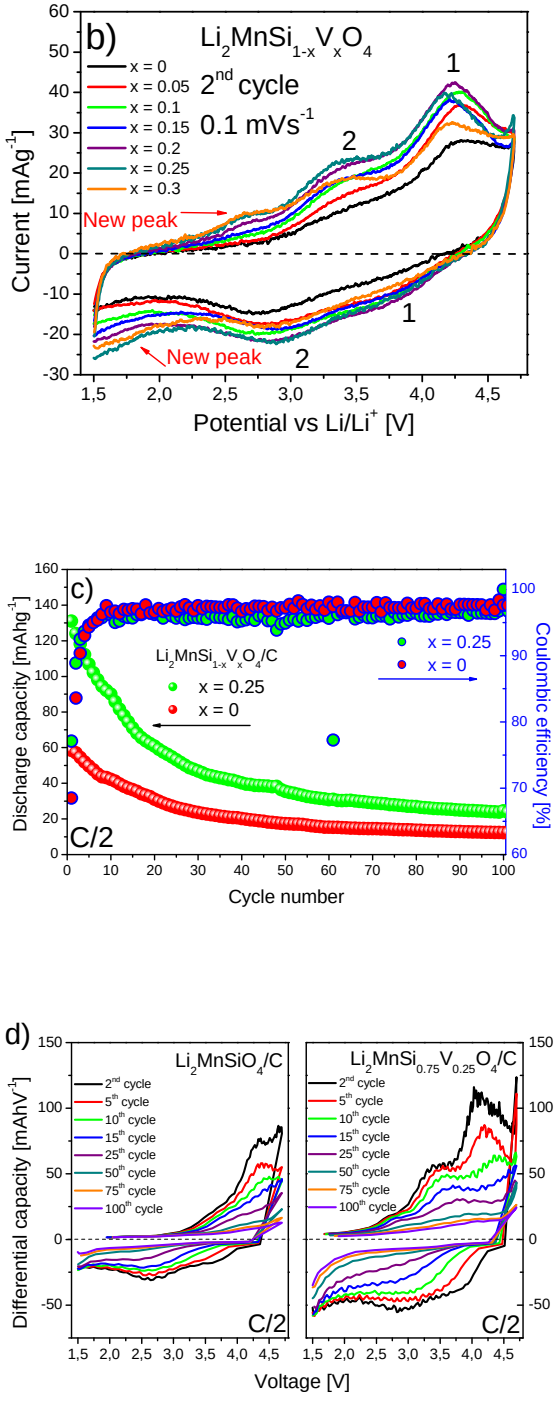

Figure 10: Cyclic voltammograms of $Li_2MnSi_{1-x}V_xO_4$ ($0 \leq x \leq 0.3$) a) first cycle and b) second cycle. Scan rate was set to $0.1 mVs^{-1}$. c) Long-term cycling at C/2 of Li_2MnSiO_4 and

$Li_2MnSi_{0.75}V_{0.25}O_4$. d) Differential capacity profile of Li_2MnSiO_4 and $Li_2MnSi_{0.75}V_{0.25}O_4$ of the 2^{nd}, 5^{th}, 10^{th}, 15^{th}, 25^{th}, 50^{th}, 75^{th} and 100^{th} cycle of the long-term cycling from c).

The onset of oxidation and the center of the anodic peak are shifted to slightly lower potentials with increasing V concentration. Furthermore, the anodic peak area is increasing in the concentration series and peaking at 25 mol % V substitution. The signal for 30 mol % V substitution is reduced again, and the data is in agreement with the galvanostatic load curves. No additional signal can be detected on first oxidation. In the cathodic direction, two broad peaks are observed where the first minor peak is located at about 3.8 V and the second major peak at about 2.7 V. The splitting into two extremely broad peaks can be directly linked to the structural degradation, since the redox potential of a given cation is dependent on its chemical environment. In this case the first minor peak is believed to correspond to Mn still in its initial coordination, while the second major peak at lower potential displays Mn in an altered environment and possibly in a different coordination. For V substituted samples both peaks are shifted to slightly higher potentials, which could be caused by a decreased overpotential. Interestingly, an additional peak appears at potentials close to the cut off potential. Upon the second anodic polarization, the reference sample shows two broad anodic peaks, one obvious and the other one barely visible. The same peaks are observable for the V substituted samples, with the same increasing behavior as described for the first cycle. In addition, also a new anodic peak, of increasing intensity within the concentration series, at about 2.7 V is observed. The subsequent cathodic polarization reassembles the first cycle qualitatively, where V substituted samples show an increased response, and the additional peak at relatively low potentials. CV and differential capacity studies in literature never reported redox activity at low potentials for

Li_2MnSiO_4. [12,44–48] Furthermore, the potential region of these additional anodic and cathodic signals lies in the region of the second lithiation and delithiation of V_2O_5. [49] Liivat and Thomas calculated the redox potential of $V^{4+/}V^{5+}$ vs. Li/Li^+ to be 2.1 V in a hypothetical Li_2FeVO_4 structure. [29] The increasing intensity of the peak, especially visible in anodic direction, in combination with literature, strongly suggests V to be redox active $Li_2MnSi_{1-x}V_xO_4$, but cannot explain why no additional anodic peak was observed upon the first oxidation. Further studies are required to verify these findings. The long-term cycling of the reference and the 25 mol % V substituted sample showed a strong decay in discharge capacity upon cycling for both samples, while the coulombic efficiency reaches values between 95 and 100% after the first few cycles. After 20 cycles the reference sample and the 25 mol % V substituted sample showed capacity retentions of 50% and 46%, respectively. During later cycles the sloping profile is less pronounced, but still present. The experiment was terminated after 100 cycles. The remaining discharge capacity was 12 and 25 $mAhg^{-1}$ for the reference and the 25 mol % V substituted samples, respectively. It was pointed out in the introduction that changes in the Mn coordination cause the capacity decay, hence the rate of degradation can be directly linked to the amount of Li extracted or in other words, the amount of Mn oxidized to a higher valence during each charge cycle. Since V was found not to substitute Mn, V substitution does not mitigate the structural degradation. Differential capacity profiles of selected cycles for both samples were derived. The first plot shows the 2^{nd} cycle. It qualitatively reassembles the CV curves. Also here, the additional anodic and cathodic peaks of the V substituted sample, located at about 2.7 V and close to cut-off, respectively, are visible. But it is obvious that in both cases all peaks are decreasing upon cycling, and almost all visible Mn redox activity disappears after prolonged cycling. In order to understand how V substitution influences the charge transfer resistance and

the Li diffusion of Li_2MnSiO_4, the materials were further analyzed by AC impedance spectroscopy. The Nyquist representation with the suggested equivalent circuit model in the inset is given in Figure 11 a). Figure 11 b) shows the dependence of Z_{Re} on $\omega^{-1/2}$ in the range were Z_{Re} and Z_{Im} are parallel. This region was not the same for all samples. The slope of Z_{Re} against $\omega^{-1/2}$ is related to the diffusion, in the range where Z_{Re} and Z_{im} are in parallel when plotted against $\omega^{-1/2}$. [50] The AC impedance spectra consisted in all cases of a depressed semi-circle in the high frequency region followed by a line profile. The data can be described by a modified Randles circuit. The first resistor, R_e, accounts for the electrolyte resistance. The next components in parallel are a resistor, accounting for the charge transfer resistance $R_{ct,}$ and a constant phase element (CPE), related to the double layer capacitance Q_{dl}. The CPE in parallel to the resistor (Cole element) was chosen to describe the depressed profile of the semi-circle, which is caused by an inhomogeneous current density distribution due to the porous structure. The low frequency part of the impedance spectra was fitted by an open circuit terminus Generalized Finite Warburg element W_o.

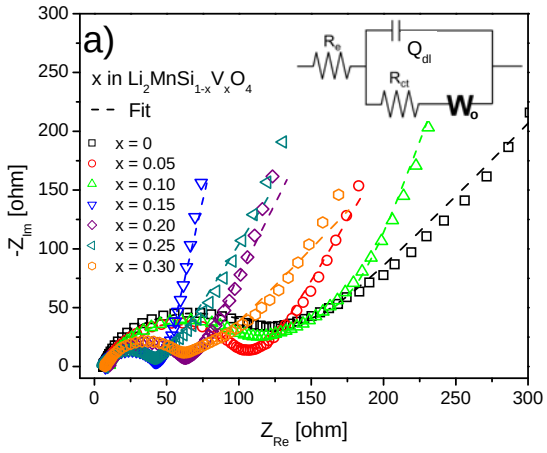

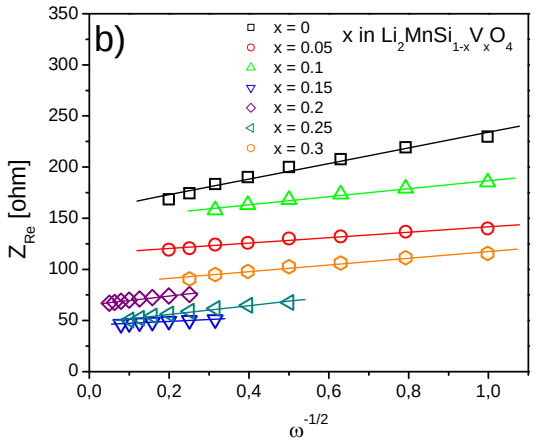

Figure 11: AC impedance data of $Li_2MnSi_{1-x}V_xO_4$ ($0 \leq x \leq 0.3$). a) Nyquist representation including the fitted line and the equivalent circuit. b) Z_{Re} vs. $\omega^{-1/2}$.

The values of R_e, R_{ct} and Li diffusion coefficient (D_{Li}) are given in Table 2. The diffusion coefficient was calculated according to a Warburg model with a linear overvoltage-current relationship [50,51] using the following equation: [52,53]

$$D = \frac{R^2T^2}{2A^2n^4F^4C_{Li}{}^2\sigma^2} \qquad (1)$$

Where R and T are the universal gas constant and the absolute temperature, respectively, A is the surface area of the electrode, n the number of electrons in the electrochemical reaction (1 for Li), F is the Faraday constant, and C_{Li} is the Li ion concentration in the material. C_{Li} can described as the quotient of density and molar mass, multiplied by a factor 2 to account for 2 Li per formula unit. In this case it was assumed that the substituted materials are identical with the desired nominal compositions. The lattice parameters given in Table 1 were applied to calculate the crystal density of each sample. The parameter σ is the slope of Z_{Re} vs. $\omega^{-1/2}$ in the range where Z_{Re} and Z_{Im} are parallel.

Table 2: Electrolyte and charge transfer resistance and calculated Li diffusion coefficients from AC impedance data of $Li_2MnSi_{1-x}V_xO_4$ ($0 \leq x \leq 0.3$).

x in $Li_2MnSi_{1-x}V_xO_4$	**[1] R_e [Ohm]**	**[1] R_{ct} [Ohm]**	**[2] D_{Li} [cm^2s^{-1}]**
0	6.312 (1.11%)	84.31 (3.42%)	9.7E-16
0.05	8.08 (0.76%)	86.43 (0.89%)	8.1E-15
0.1	8.86 (0.85%)	95.41 (1.31%)	3.6E-15
0.15	7.61 (1.20%)	31.88 (1.36%)	1.6E-14
0.2	9.51 (0.82%)	49.29 (1.16%)	3.1E-15
0.25	6.78 (0.84%)	24.76 (1.78%)	3.0E-15
0.3	7.71 (1.12%)	43.49 (1.18%)	5.2E-15

[1] Uncertainty given in brackets. [2] Assumptions are described in the main text.

Table 2 shows that V substitution influences the charge transfer resistance and the Li diffusion coefficient. The results are in agreement with the galvanostatic cycling experiments and CV measurements. A decreased charge transfer resistance is observable for V substitution levels ≥ 15 mol %. The lowered charge transfer is probably caused by VO_4 units interrupting the strongly insulating SiO_4 framework. The STEM EELS analysis revealed the strongly inhomogeneous distribution of V, which most probably makes every sample unique and hence could explain inconsistences in the R_{ct} values. Discussed strain, stacking faults and defects in the structure seem to also positively influence the diffusion coefficient for Li ions, which for all V substituted samples is increased by one order of magnitude and is in the range of E-15 cm^2s^{-1}. The exact values have to be taken with caution due to the assumptions made about the crystal density and the Warburg model. Hence the data should be read as a trend and the reported range seems

reasonable. Galvanostatic cycling at elevated rates also strongly suggests increased Li diffusion for V substituted samples.

Conclusions

In-depth investigations concerning the feasibility of substituting V for Mn or Si in Li_2MnSiO_4 were performed. A sol-gel method was employed and samples with the nominal compositions $Li_2Mn_{1-x}V_xSiO_4$ ($0 \leq x \leq 0.2$) and $Li_2MnSi_{1-x}V_xO_4$ ($0 \leq x \leq 0.3$) were synthesized. The Li_2MnSiO_4 reference was indexed and fitted to a β_{II} *Pmn2₁* model. V substitution on the Mn-site was shown to cause phase separation and V exclusion at V concentrations ≥ 10 mol %. An increasing amount of a V containing spinel phase and Li_2SiO_3 was detected. The substitution onto the Si-site caused increased misfits in the patterns suggesting disorder. But, overall the system could still be identified by the space group *Pmn2₁*. STEM EELS revealed inhomogeneous distributions of V, which was mainly present in a tetravalent state. Dependent on the concentration, some lower valence V at lower concentrations and higher valence V at higher concentrations were detected. These findings suggest varying local compositions. Furthermore, XRD and STEM EELS revealed a secondary MnO phase to be more correctly addressed as $Mn_{1-x}V_yO$ ($1-x+y < 1$). This phase is believed to be caused either by a limited solid solubility of the system, or induced by the thermal history of the sample. The $Li_2MnSi_{1-x}V_xO_4$ ($0 \leq x \leq 0.3$) structures were shown to offer superior electrochemical properties compared to the reference and to the $Li_2Mn_{1-x}V_xSiO_4$ ($0 \leq x \leq 0.2$) samples. The discharge capacity was highest for the nominal composition $Li_2MnSi_{0.75}V_{0.25}O_4$, which reached 160 $mAhg^{-1}$ in the initial cycle. This value corresponds roughly to the 1 Li per formula unit reaction and was 40% higher than the reference

sample. Additional redox activity which could be attributed to the V^{4+}/V^{5+} redox couple was revealed by CV measurements. EIS spectra showed decreased charge transfer resistance and increased values for Li diffusion. V does not substitute Mn and hence no effect on the structural instability upon cycling was detected and *in situ* XRD analysis showed amorphization for both the substituted and the reference sample.

Acknowledgements

The research council of Norway is gratefully acknowledged for funding the SilicatBatt project (grant number: 216469/E20). TEM characterization was supported by the project NORTEM (Grant 197405) within the program INFRASTRUCTURE of the Research Council of Norway (RCN). NORTEM was co-funded by the RCN and the project partners NTNU, UiO and SINTEF.

References

(1) Nytén, A.; Abouimrane, A.; Armand, M.; Gustafsson, T.; Thomas, J. O. Electrochemical Performance of Li_2FeSiO_4 as a New Li-Battery Cathode Material. *Electrochem. commun.* **2005**, *7* (2), 156–160.

(2) Dominko, R.; Bele, M.; Gaberšček, M.; Meden, A.; Remškar, M.; Jamnik, J. Structure and Electrochemical Performance of Li_2MnSiO_4 and Li_2FeSiO_4 as Potential Li-Battery Cathode Materials. *Electrochem. commun.* **2006**, *8* (2), 217–222.

(3) Ellis, B. L.; Lee, K. T.; Nazar, L. F. Positive Electrode Materials for Li-Ion and Li-Batteries. *Chem. Mater.* **2010**, *22* (3), 691–714.

(4) Islam, M. S.; Dominko, R.; Masquelier, C.; Sirisopanaporn, C.; Armstrong, A. R.; Bruce,

P. G. Silicate Cathodes for Lithium Batteries: Alternatives to Phosphates? *J. Mater. Chem.* **2011**, *21*, 9811–9818.

(5) Kuganathan, N.; Islam, M. S. Li_2MnSiO_4 Lithium Battery Material: Atomic-Scale Study of Defects, Lithium Mobility, and Trivalent Dopants. *Chem. Mater.* **2009**, *21* (21), 5196–5202.

(6) Politaev, V. V.; Petrenko, A. A.; Nalbandyan, V. B.; Medvedev, B. S.; Shvetsova, E. S. Crystal Structure, Phase Relations and Electrochemical Properties of Monoclinic Li_2MnSiO_4. *J. Solid State Chem.* **2007**, *180* (3), 1045–1050.

(7) Duncan, H.; Kondamreddy, A.; Mercier, P. H. J.; Le Page, Y.; Abu-Lebdeh, Y.; Couillard, M.; Whitfield, P. S.; Davidson, I. J. Novel Pn Polymorph for Li_2MnSiO_4 and Its Electrochemical Activity As a Cathode Material in Li-Ion Batteries. *Chem. Mater.* **2011**, *23* (24), 5446–5456.

(8) Gummow, R. J.; Sharma, N.; Peterson, V. K.; He, Y. Crystal Chemistry of the Pmnb Polymorph of Li_2MnSiO_4. *J. Solid State Chem.* **2012**, *188*, 32–37.

(9) Gummow, R. J.; He, Y. Recent Progress in the Development of Li_2MnSiO_4 Cathode Materials. *J. Power Sources* **2014**, *253*, 315–331.

(10) Saracibar, A.; Wang, Z.; Carroll, K. J.; Meng, Y. S.; Dompablo, M. E. A. New Insights into the Electrochemical Performance of Li_2MnSiO_4 : Effect of Cationic Substitutions. *J. Mater. Chem. A* **2015**, *3*, 6004–6011.

(11) Yi, T.; Li, Y.; Cheng, X.; Zhang, Y. Local Structure Evolution of Li2Fe0.5Mn0.5SiO4 during Delithiation/lithiation Processes: A First-Principles Investigation. *Comput. Mater. Sci.* **2015**, *99*, 96–104.

(12) Świętosławski, M.; Molenda, M.; Furczoń, K.; Dziembaj, R. Nanocomposite C/Li_2MnSiO_4 Cathode Material for Lithium Ion Batteries. *J. Power Sources* **2013**, *244*, 510–514.

(13) Hwang, C.; Kim, T.; Noh, Y.; Cha, W.; Shim, J.; Kwak, K.; Ok, K. M.; Lee, K.-K. Synthesis, Characterization, and Electrochemical Performance of V-Doped Li_2MnSiO_4/C Composites for Li-Ion Battery. *Mater. Lett.* **2015**.

(14) Hao, H.; Wang, J.; Liu, J.; Huang, T.; Yu, A. Synthesis, Characterization and Electrochemical Performance of Li_2FeSiO_4/C Cathode Materials Doped by Vanadium at Fe/Si Sites for Lithium Ion Batteries. *J. Power Sources* **2012**, *210*, 397–401.

(15) Bajars, G.; Kucinskis, G.; Smits, J.; Kleperis, J.; Lusis, A. Characterization of $LiFePO_4$/C Composite Thin Films Using Electrochemical Impedance Spectroscopy. *IOP Conf. Ser. Mater. Sci. Eng.* **2012**, *38*, 012019.

(16) Moskon, J.; Dominko, R.; Cerc-Korosec, R.; Gaberscek, M.; Jamnik, J. Morphology and Electrical Properties of Conductive Carbon Coatings for Cathode Materials. *J. Power Sources* **2007**, *174* (2), 683–688.

(17) Dominko, R. Li_2MSiO_4 (M = Fe And/or Mn) Cathode Materials. *J. Power Sources* **2008**, *184* (2), 462–468.

(18) Chen, R.; Heinzmann, R.; Mangold, S.; Chakravadhanula, V. S. K.; Hahn, H.; Indris, S. Structural Evolution of $Li_2Fe_{1-y}Mn_ySiO_4$ (y = 0, 0.2, 0.5, 1) Cathode Materials for Li-Ion Batteries upon Electrochemical Cycling. *J. Phys. Chem. C* **2013**, *117*, 884–893.

(19) Deng, C.; Zhang, S.; Yang, S. Y. Effect of Mn Substitution on the Structural, Morphological and Electrochemical Behaviors of $Li_2Fe_{1-x}Mn_xSiO_4$ Synthesized via Citric Acid Assisted Sol-Gel Method. *J. Alloys Compd.* **2009**, *487* (1-2), 18–23.

(20) Guo, H.; Cao, X.; Li, X.; Li, L.; Li, X.; Wang, Z.; Peng, W.; Li, Q. Optimum Synthesis of $Li_2Fe_{1-x}Mn_xSiO_4$/C Cathode for Lithium Ion Batteries. *Electrochim. Acta* **2010**, *55* (27), 8036–8042.

(21) Kokalj, A.; Dominko, R.; Mali, G.; Meden, A.; Gaberscek, M.; Jamnik, J. Beyond One-Electron Reaction in Li Cathode Materials: Designing $Li_2Mn_xFe_{1-x}SiO_4$. *Chem. Mater.* **2007**, *19* (15), 3633–3640.

(22) Rangappa, D.; Murukanahally, K. D.; Tomai, T.; Unemoto, A.; Honma, I. Ultrathin Nanosheets of Li_2MSiO_4(M = Fe, Mn) as High-Capacity Li- Ion Battery Electrode. *Nano* **2012**, *4*.

(23) Shao, B.; Abe, Y.; Taniguchi, I. Synthesis and Electrochemical Characterization of $Li_2Fe_xMn_{1-x}SiO_4$/C ($0 \leqq x \leqq 0.8$) Nanocomposite Cathode for Lithium-Ion Batteries. *Powder Technol.* **2013**, *235*, 1–8.

(24) Wagner, N.; Dalod, A.; Svensson, A.; Vullum-Bruer, F. Fe and V Substituted Li_2MnSiO_4/C as Potential Cathode Material for Li-Ion Batteries. *ECS Trans.* **2015**, *64* (22), 33–45.

(25) West, K.; Zachau-Christiansen, B.; T., J. Thin-Film Vanadium Batteries Oxide Electrodes for Lithium Batteries. *J. Power Sources* **1993**, 127–134.

(26) Dong, W.; Rolison, D. R.; Dunn, B. Electrochemical Properties of High Surface Area Vanadium Oxide Aerogels. *Electrochem. Solid State Lett.* **2001**, *3*, 457–459.

(27) Tarascon, J. M.; Armand, M. Issues and Challenges Facing Rechargeable Lithium Batteries. *Nature* **2001**, *414* (6861), 359–367.

(28) Li, Y.; Cheng, X.; Zhang, Y. Achieving High Capacity by Vanadium Substitution into Li_2FeSiO_4. *J. Electrochem. Soc.* **2012**, *159* (2), A69.

(29) Liivat, A.; Thomas, J. O. A DFT Study of Polyanion Substitution into the Li-Ion Battery Cathode Material Li_2FeSiO_4. *Comput. Mater. Sci.* **2010**, *50* (1), 191–197.

(30) Hong, Y.; Ying, Z.; Xuan, C. Effect of Vanadium Substitution on Structure of Li_2FeSiO_4 /C Composites. *JOURNALOF Electrochem.* **2013**, *19* (6), 565–570.

(31) Zhang, L.-L.; Sun, H.-B.; Yang, X.-L.; Wen, Y.-W.; Huang, Y.-H.; Li, M.; Peng, G.; Tao, H.-C.; Ni, S.-B.; Liang, G. Study on Electrochemical Performance and Mechanism of V-Doped Li_2FeSiO_4 Cathode Material for Li-Ion Batteries. *Electrochim. Acta* **2015**, *152*, 496–504.

(32) Deng, C.; Zhang, S.; Wu, Y. X.; Zhao, B. D. Partial Substitution of Mn/Si with V, Cr or Al in Li_2MnSiO_4 Nanoparticle: Dependence of the Physical and Electrochemical

Properties on the Substitution Strategy. *J. Electroanal. Chem.* **2014**, *719*, 150–157.

(33) Wagner, N.; Svensson, A.-M.; Vullum-Bruer, F. Effect of Carbon Content and Annealing Atmosphere on Phase Purity and Morphology of Li_2MnSiO_4 Synthesized by a PVA Assisted Sol–gel Method. *Solid State Ionics* **2015**, *276*, 26–32.

(34) Li, Y.-X.; Gong, Z.-L.; Yang, Y. Synthesis and Characterization of Li_2MnSiO_4/C Nanocomposite Cathode Material for Lithium Ion Batteries. *J. Power Sources* **2007**, *174* (2), 528–532.

(35) Manoubi, T.; Tencé, M.; Walls, M. G.; Colliex, C.; Solides, P.; Cedex, O. Curve Fitting Methods for Quantitative Energy Loss Spectroscopy Analysis in Electron. *Microsc. Microanal. Microstruct.* **1990**, *1* (1), 23–39.

(36) de la Pea, F.; Burdet, P.; Ostasevicius, T.; Sarahan, M.; Nord, M.; Fauske, V. T.; Taillon, J.; Eljarrat, A.; Mazzucco, S.; Donval, G.; et al. HyperSpy.

(37) Ahn, C. C.; Rez, P. Inner Shell Edge Profiles in Electron Energy Loss Spectroscopy. *Ultramicroscopy* **1985**, *17*, 105–115.

(38) Plumier, R.; Sougi, M. Observation of a First-Order Transition at T<Tc in MnV_2O_4. *Phys. B Condens. Matter* **1989**, *155*, 315–319.

(39) Armstrong, A. R.; Kuganathan, N.; Islam, M. S.; Bruce, P. G. Structure and Lithium Transport Pathways in Li_2FeSiO_4 Cathodes for Lithium Batteries. *J. Am. Chem. Soc.* **2011**, *133*, 13031–13035.

(40) Su, D. S. Electron Beam Induced Changes in Transition Metal Oxides. *Anal Bioanal Chem* **2002**, *374* (4), 732–735.

(41) Su, D. S.; Wieske, M.; Beckmann, E.; Blume, A.; Mestl, G.; Schloegl, R. Reduction of V_2O_5 in the Transmission Electron Microscope. *Catal. Letters* **2001**, *1* (2), 81–86.

(42) Tan, H.; Verbeeck, J.; Abakumov, A.; Van Tendeloo, G. Oxidation State and Chemical Shift Investigation in Transition Metal Oxides by EELS. *Ultramicroscopy* **2012**, *116*, 24–33.

(43) Rossell, M. D.; Agrawal, P.; Borgschulte, A.; Hébert, C.; Passerone, D.; Erni, R. Direct Evidence of Surface Reduction in Monoclinic $BiVO_4$. *Chem. Mater.* **2015**, 150414110704005.

(44) Wagner, N.; Svensson, A.-M.; Vullum-Bruer, F. Liquid Feed Flame Spray Pyrolysis as Alternative Synthesis for Electrochemically Active Nanosized Li2MnSiO4. *Trans. Mater. Res.* **2016**, *accepted m*.

(45) Sun, D.; Wang, H.; Ding, P.; Zhou, N.; Huang, X.; Tan, S.; Tang, Y. In-Situ Synthesis of Carbon Coated Li_2MnSiO_4 Nanoparticles with High Rate Performance. *J. Power Sources* **2013**, *242*, 865–871.

(46) Wang, M.; Yang, M.; Ma, L.; Shen, X.; Zhang, X. Structural Evolution and Electrochemical Performance of Li_2MnSiO_4/C Nanocomposite as Cathode Material for Li-Ion Batteries. *J. Nanomater.* **2014**, *2014*, 1–6.

(47) Muraliganth, T.; Stroukoff, K. R.; Manthiram, A. Microwave-Solvothermal Synthesis of

Nanostructured Li_2MSiO_4/C (M = Mn and Fe) Cathodes for Lithium-Ion Batteries. *Chem. Mater.* **2010**, *22* (20), 5754–5761.

(48) Bhaskar, A.; Deepa, M.; Rao, T. N.; Varadaraju, U. V. In Situ Carbon Coated Li2MnSiO4/C Composites as Cathodes for Enhanced Performance Li-Ion Batteries. *J. Electrochem. Soc.* **2012**, *159* (12), A1954–A1960.

(49) Zhang, X.-F.; Wang, K.-X.; Wei, X.; Chen, J.-S. Carbon-Coated V2O5 Nanocrystals as High Performance Cathode Material for Lithium Ion Batteries. *Chem. Mater.* **2011**, 5290–5292.

(50) Meyers, J. P.; Doyle, M.; Darling, R. M.; Newman, J. The Impedance Response of a Porous Electrode Composed of Intercalation Particles. *J. Electrochem. Soc.* **2000**, *147* (8), 2930.

(51) Bard, A. J.; Faulkner, L. R. *ELECTROCHEMICAL METHODS: Fundamentals and Applications*, 2nd Edition.; John Wiley and Sons, INC., 2001.

(52) Zhang, L.-L.; Duan, S.; Yang, X.-L.; Peng, G.; Liang, G.; Huang, Y.-H.; Jiang, Y.; Ni, S.-B.; Li, M. Reduced Graphene Oxide Modified Li_2FeSiO_4/C Composite with Enhanced Electrochemical Performance as Cathode Material for Lithium Ion Batteries. *ACS Appl. Mater. Interfaces* **2013**, *5*, 12304–12309.

(53) Wang, X.; Hao, H.; Liu, J.; Huang, T.; Yu, A. A Novel Method for Preparation of Macroposous Lithium Nickel Manganese Oxygen as Cathode Material for Lithium Ion Batteries. *Electrochim. Acta* **2011**, *56* (11), 4065–4069.

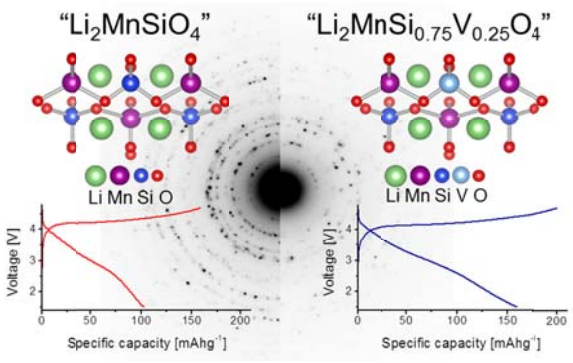
"Li2MnSiO4"
"Li2MnSi0.75V0.25O4"
Li Mn Si O
Li Mn Si V O
Voltage [V]
Specific capacity [mAhg-1]